AGU PUBLICATIONS

Geophysical Research Letters

RESEARCH LETTER
10.1002/2017GL072545

Key Points:
- The 2016 Ecuador earthquake (M_w 7.8) is similar to the 1942 event (M_w 7.8) which was followed by 1958 (M_w 7.7) and 1979 (M_w 8.2) events
- While teleseismic inversion was neutral about inclusion or exclusion of slip shallower than 15 km, observed tsunamis favored the latter
- Final fault had a maximum slip of 2.5 m and a large-slip area of 80 km (strike wise) times 60 km (dip wise) in the depth range of 15–35 km

Supporting Information:
- Supporting Information S1

Correspondence to:
M. Heidarzadeh,
mohammad.heidarzadeh@brunel.ac.uk

Citation:
Heidarzadeh, M., S. Murotani, K. Satake, T. Takagawa, and T. Saito (2017), Fault size and depth extent of the Ecuador earthquake (M_w 7.8) of 16 April 2016 from teleseismic and tsunami data, *Geophys. Res. Lett.*, *44*, 2211–2219, doi:10.1002/2017GL072545.

Received 7 SEP 2016
Accepted 24 FEB 2017
Accepted article online 28 FEB 2017
Published online 11 MAR 2017

Fault size and depth extent of the Ecuador earthquake (M_w 7.8) of 16 April 2016 from teleseismic and tsunami data

Mohammad Heidarzadeh[1], Satoko Murotani[2], Kenji Satake[3], Tomohiro Takagawa[4], and Tatsuhiko Saito[5]

[1]Division of Civil Engineering, Department of Mechanical, Aerospace and Civil Engineering, Brunel University London, Uxbridge, UK, [2]National Museum of Nature and Science, Tsukuba, Japan, [3]Earthquake Research Institute, University of Tokyo, Tokyo, Japan, [4]Port and Airport Research Institute, Yokosuka, Japan, [5]National Research Institute for Earth Science and Disaster Resilience, Tsukuba, Japan

Abstract The April 2016 Ecuador M_w 7.8 earthquake was the first megathrust tsunamigenic earthquake along the Ecuador-Colombia subduction zone since 1979 (M_w 8.2 with 200 deaths from tsunami). While there was no tsunami damage from the 2016 earthquake, small tsunamis were recorded at Deep-ocean Assessment and Reporting of Tsunami and tide gauges. Here we designed various fault models with and without shallow-slip area and compared the computed teleseismic and tsunami waveforms with the observations. While teleseismic inversions were indifferent about inclusion or exclusion of the shallow slip, tsunami waveforms strongly favored the slip model without shallow slip. Our final slip model has a depth range of 15–44 km, and its western shallowest limit is located at the distance of ~60 km from the trench. Maximum and average slips were 2.5 and 0.7 m, respectively. The large-slip area was 80 km (along strike) × 60 km (along dip) in the depth range of 15–35 km.

1. Introduction

A large thrust earthquake occurred on 16 April 2016 onshore Ecuador. The origin time of the earthquake was 23:58:36 UTC with an epicenter located at 79.922°W and 0.382°N (Figure 1) according to the United States Geological Survey (USGS). The earthquake depth was ~21 km having a moment magnitude (M_w) of 7.8. Based on various news reports, several nearby towns and population centers were severely damaged resulting in a death toll of ~660 people due to the earthquake. The resulting tsunami was small registering a maximum tide-gauge amplitude of ~10 cm (Figure 1d). Although the tsunami did not cause any damage, the tsunami signals were clear on three tide gauges and three Deep-ocean Assessment and Reporting of Tsunami (DART) gauges providing valuable information to study the source of the earthquake (Figure 1d). Tsunami amplitudes were 0.5–2 cm on DARTs.

The 2016 Ecuador earthquake was the result of the subduction of the Nazca plate beneath the South American plate at a rate of 2.5 to 4.6 cm/yr offshore Ecuador and Colombia [*Trenkamp et al.*, 2002; *Ye et al.*, 2016a, 2016b]. The Ecuador-Colombia coast has experienced four megathrust tsunamigenic earthquakes since 1900 A.D.: the events of 1906 (M_w 8.8), 1942 (M_w 7.8), 1958 (M_w 7.7), and 1979 (M_w 8.2) [*Kanamori and McNally*, 1982; *Collot et al.*, 2004; *Arreaga-Vargas et al.*, 2005] (see Figure 1c for locations and rupture zones). A northward rupture migration can be seen for the rupture zones of the 1942, 1958, and 1979 earthquakes (Figure 1c). These previous earthquakes were tsunamigenic and caused tsunami damage. The casualties due to the 1906 tsunami were estimated at 500–1500 by *Soloviev and Go* [1975]. The 1942 and 1958 tsunamis were moderate with minimal damage and a few deaths [*Soloviev and Go*, 1975]. The 1979 tsunami caused at least 200 deaths along the coast of Colombia [*Arreaga-Vargas et al.*, 2005].

The 2016 event is important because it is among the largest damaging earthquakes to hit the area in decades. Furthermore, its size is similar to that of the 1942 event (both M_w 7.8), and the aftershock distribution well covers the rupture zone of the 1942 event (Figure 1c); hence, a northward stress transfer from this large earthquake could possibly trigger future large earthquakes to the north of the 2016 epicenter in a way similar to the northward migrations of the 1942, 1958, and 1979 epicenters (Figure 1c). Although rupture patterns along subduction plate boundaries are far unpredictable [*Ando*, 1975; *Satake and Atwater*, 2007; *Stein and Okal*, 2007], unilateral stress transfer was observed in other subduction zones, e.g., southward stress

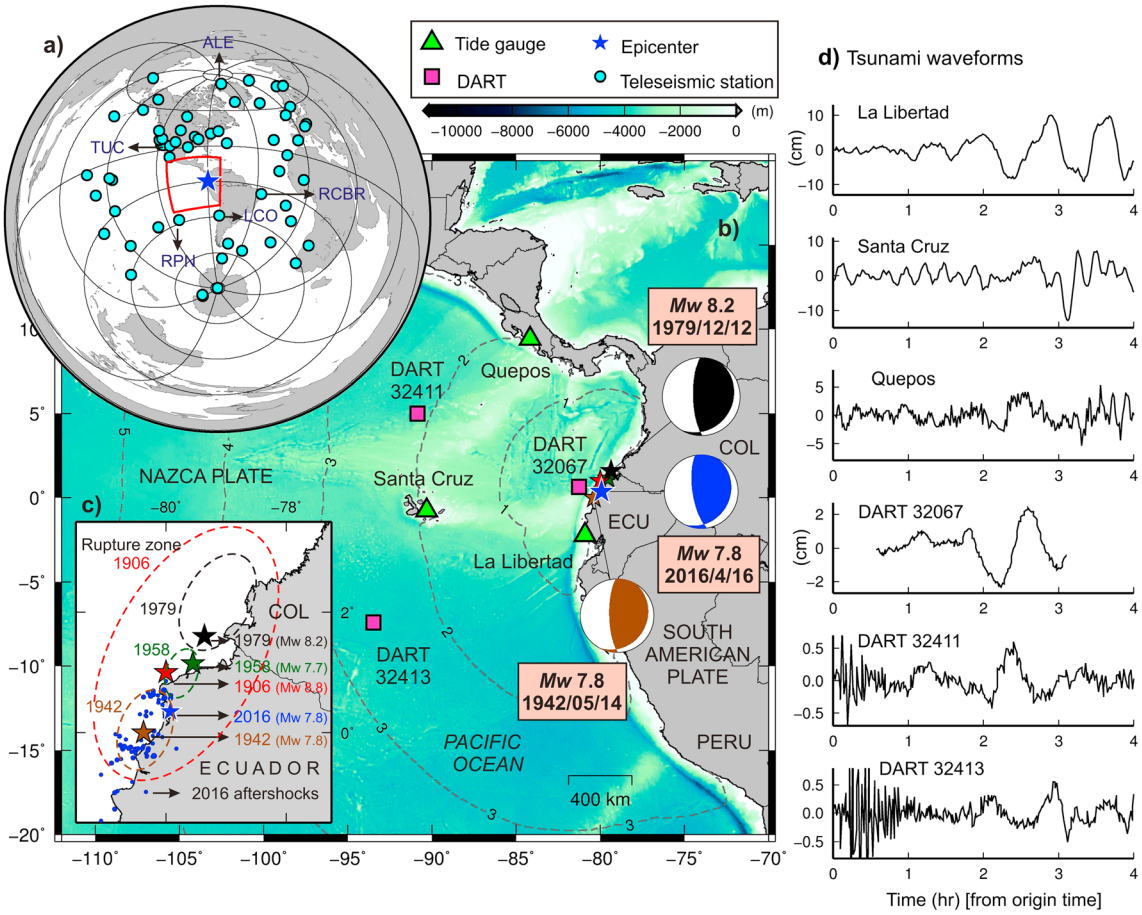

Figure 1. General location map showing locations of previous large earthquakes as well as teleseismic and tsunami stations used in this study. (a) Locations of teleseismic stations. The five stations accompanied with names are those shown in Figures 2 and 3. (b) Epicenters of the 2016 (blue star) and previous earthquakes along the Ecuador-Colombia coast and locations of DART and tide gauge stations. Dashed lines are tsunami traveltime contours in hours. Focal mechanism of the 2016 event is from USGS, while those of 1979 and 1942 are from *Kanamori and Given* [1981] and *Swenson and Beck* [1996], respectively. (c) Epicenters and rupture zones of previous large earthquakes based on *Kanamori and McNally* [1982]. The dashed ellipses show approximations of the earthquake rupture zones according to *Kanamori and McNally* [1982]. Blue solid circles show 1 week aftershocks ($M > 4$) of the 2016 earthquake from the USGS catalog. ECU and COL stand for Ecuador and Colombia. (d) Tsunami waveforms due to the 16 April 2016 event. The first 30 min of the DART 32067 record is not available.

transfer from the 2004 Sumatra-Andaman M_w 9.2 earthquake [*McCloskey et al.*, 2005] to the 2005 Nias M_w 8.7 [*Kreemer et al.*, 2006] and then to the 2007 Bengkulu M_w 8.4 [*Fujii and Satake*, 2008] megathrust tsunamigenic earthquakes. Here we use teleseismic and tsunami records of the 16 April 2016 event and employ teleseismic inversions and tsunami simulations to constrain the earthquake source. We present a source model which is consistent with both teleseismic and tsunami observations.

2. Data and Methods

In recent years, it has been shown that tsunami observations contain valuable information about earthquake sources; thus, a combination of seismic and tsunami observations has been used to obtain source models of large subduction zone earthquakes [*Satake*, 1987; *Yamazaki et al.*, 2011; *Lay et al.*, 2014; *Inazu and Saito*, 2014; *Gusman et al.*, 2015; *Li et al.*, 2016; *Heidarzadeh et al.*, 2015, 2016a, 2016b]. We applied such a method in this study. Our data consisted of 61 teleseismic and 6 tsunami records (see Figure 1 for locations). The teleseismic records were a combination of 58 *P* (vertical component) in the distance range of 30–100 arc deg and three *SH* waves in the distance range of 40–60 arc deg from the epicenter (Figure 1a). The three *SH* waves were weighted by a factor of 0.3, while the 58 *P* waves were assigned a weight factor of 1.0. The tsunami data included three DART and three tide gauge records (Figure 1d). The teleseismic records were band pass filtered (0.003–1.0 Hz), and the tsunami records were detided by estimating the tides using polynomial fitting.

We used the program package of *Kikuchi and Kanamori* [2003] based on *Kikuchi and Kanamori* [1991] for teleseismic body wave inversion by setting the velocity structure according to *Laske et al*. [2013] (CRUST 1.0) and *Kennett et al*. [1995] (ak135). We located the fault with the strike angle of 27°, similar to the strike of the trench axis. We first assumed that fault was extended up to the trench axis and divided the fault plane into 66 subfaults (11: strike wise × 6: dip wise), covering the depth range of 9.2 to 44.1 km from the sea surface (equivalent to depth 1.2–36.1 km below seafloor). The depths reported hereafter are based on measuring from the sea surface. The length and width of each subfault were 20 km. The depths and dip angles of the subfaults were based on the SLAB 1.0 global subduction zone model [*Hayes et al*., 2012] (Figure S1 in the supporting information). As shown in the next section, we also tested limited numbers of subfaults, i.e., 55 (11 × 5) and 44 (11 × 4) subfaults on deeper parts of the plate boundary. The maximum allowed rupture time was 20.0 s by using nine triangles, each having duration of 4.0 s and overlapped for 2.0 s. Maximum rupture front velocity (hereafter simply called as rupture velocity: V_r) was varied in the range 2.0–3.0 km/s with 0.25 km/s intervals in order to investigate which V_r results in the best fit between observations and computations. We note that the maximum rupture front velocity is an assumed velocity and could be different from the physical rupture velocity which can be calculated using snapshots of the rupture propagation. We calculated the normalized root-mean-square (NRMS) misfit to quantify the match between observed and computed waveforms for both teleseismic body waves and tsunamis [*Heidarzadeh et al*., 2016a, 2016b].

Numerical modeling of tsunami was conducted using a nonlinear shallow water model by a finite difference method [*Satake*, 1995]. A single bathymetry grid having a resolution of 30 arc sec from the General Bathymetric Charts of the Oceans-2014 was used [*Intergovernmental Oceanographic Commission et al*., 2014; *Weatherall et al*., 2015]. Time step for finite difference computations was 1.0 s. Seafloor deformation was calculated using the dislocation model of *Okada* [1985]. It is usually assumed that sea surface height, which is the initial condition for tsunami simulation, is equivalent to seafloor deformation [*Synolakis*, 2003]. Therefore, we used seafloor deformation as initial condition for tsunami simulations in this study. To examine the difference between seafloor deformation and sea surface height, we applied a wavelength filter to the seafloor deformation to calculate sea surface height for one of our simulations [e.g., *Kajiura*, 1963; *Saito and Furumura*, 2009]. The *Geoware*'s [2011] software was applied for tsunami traveltime analysis.

3. Results and Discussion

We first conducted inversion of teleseismic body waves for the 66 subfaults reaching the trench axis (Figure 2), with three different assumed rupture velocities of 2.0, 2.5, and 3.0 km/s, and simulated tsunami waveforms (Figure 2). All 61 teleseismic waveforms are shown in Figure S2 for $V_r = 3.0$ km/s. Figure 2 shows that the large-slip area expands out of the epicenter by increasing the rupture velocity, while the maximum slip amount decreases. In terms of agreement between observed and synthetic teleseismic waveforms, all three models give similar results (Figure 2) with NRMS misfits of 0.485, 0.477, and 0.473 for models $V_r = 2.0$, 2.5, and 3.0 km/s, respectively. Tsunami simulations showed that the simulated waveforms are significantly different from model with $V_r = 2.0$ km/s (Figure 2a) to the model with $V_r = 2.5$ or 3.0 km/s (Figure 2c). The tsunami NRMS misfits were 1.055, 0.937, and 0.937 for models $V_r = 2.0$, 2.5, and 3.0 km/s, respectively. However, an initial early peak is observed in tsunami simulations which does not exist in observations (arrows X2 and X3 in Figure 2c). This initial early peak in simulations can be attributed to the narrow coseismic seafloor uplift to the west of the epicenter (arrow X1 in Figure 2c). This narrow uplift is the result of shallow slip located close to the trench axis. In fact, tsunami observations indicate that the slip area needs to be limited to the deeper part of the plate interface.

We then excluded the shallow subfaults and tested 55 (11 × 5) and 44 (11 × 4) subfault models covering depth ranges of 12.4–44.1 km (Figure 3b) and 14.7–44.1 km (Figure 3c), respectively. The rupture velocity is fixed at $V_r = 3.0$ km/s. Despite significant changes in fault dimensions, synthetic teleseismic waveforms remained similar for all three cases (Figures 3 and S3). The NRMS misfits from teleseismic inversions were 0.473 (for 11 × 6), 0.478 (for 11 × 5), and 0.489 (for 11 × 4) indicating that the results were very close to each other. It can be inferred from this result that the main slip region to explain the synthetic teleseismic waveforms exists at the deeper (>15 km) part of the plate interface. We also examined the downdip limit of the fault by adding a new row of blocks to the downdip end of the fault plane (i.e., 77 subfaults in 11 × 7 grid) and performing the teleseismic inversions for various V_r. Results (Figure S4) showed that the deepest row of blocks received almost no slip indicating that it can be removed, thus defining the downdip limit of the

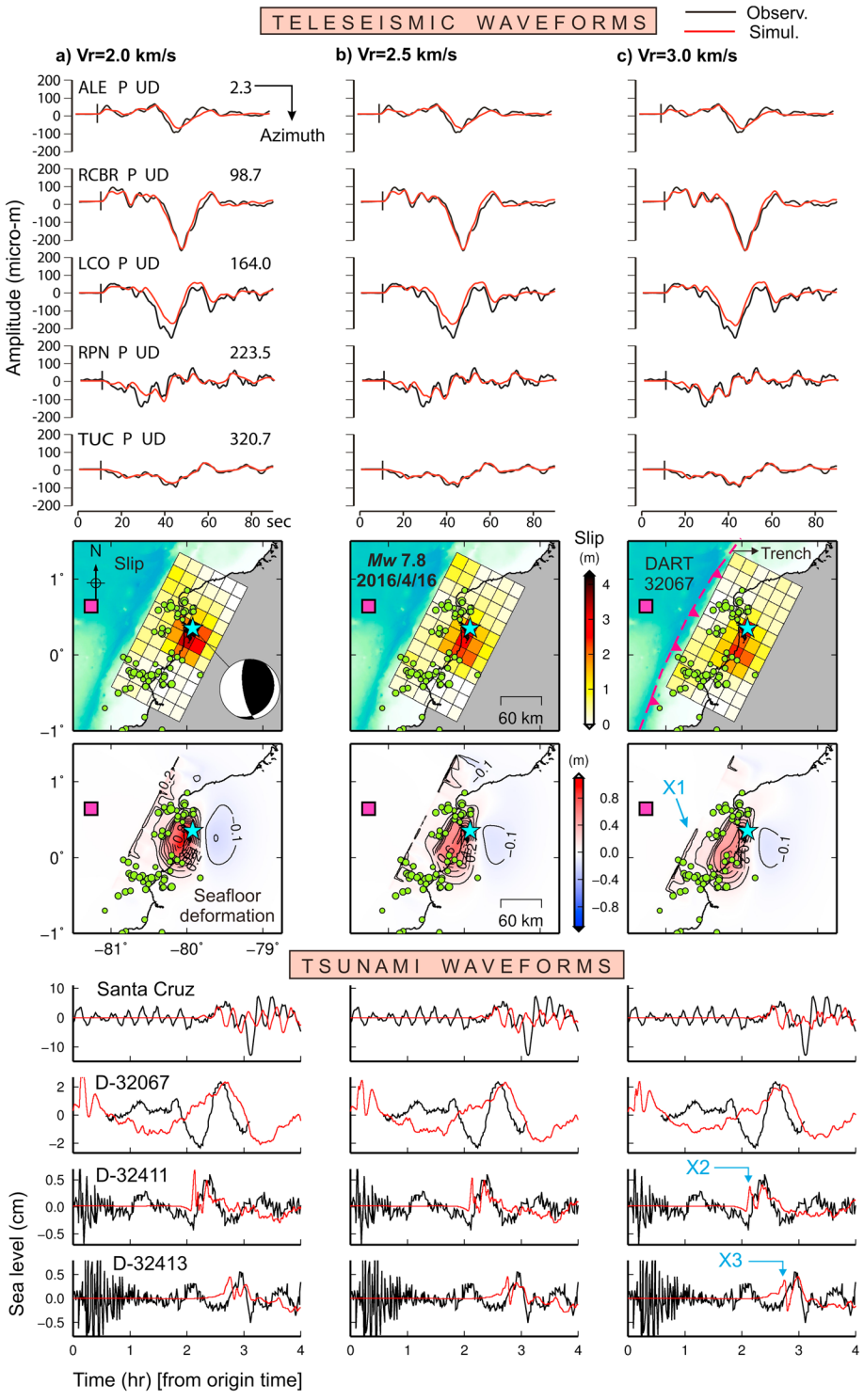

Figure 2. Seismic inversion and tsunami simulation results for a fault with slip extending up to the trench axis having 66 subfaults (strike wise: 11; dip wise: 6 subfaults). (a) From top to bottom: teleseismic waveforms (black: observations and red: synthetics), slip model, seafloor deformation, and tsunami waveforms from the model $V_r = 2.0$ km/s. (b and c) Similar to Figure 2a but for models $V_r = 2.5$ and 3.0 km/s. One week aftershocks ($M > 4$) are from the USGS catalog.

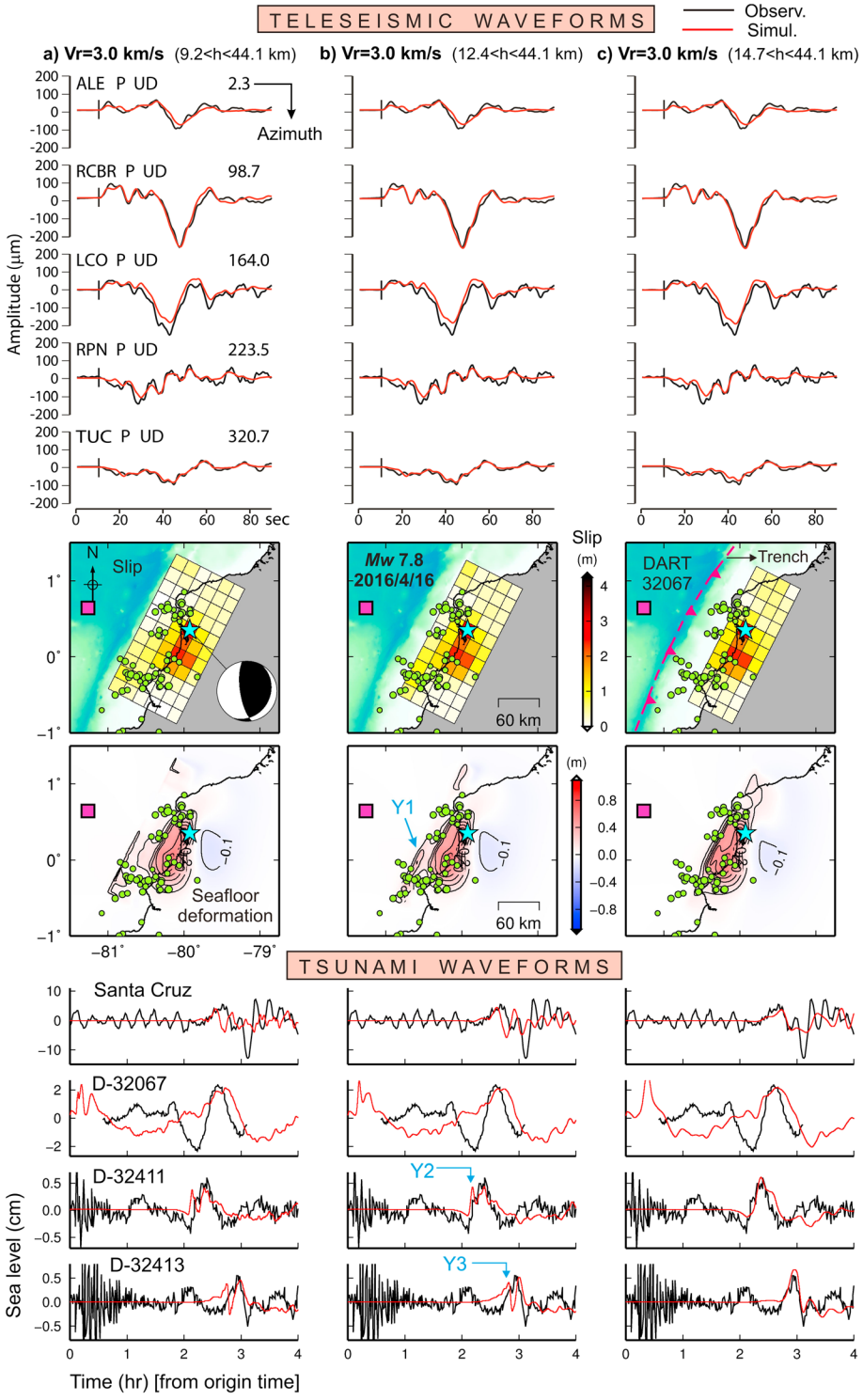

Figure 3. Seismic inversion and tsunami simulation results for faults with different fault widths. (a) From top to bottom: teleseismic waveforms (black: observations and red: synthetics), slip model, seafloor deformation, and tsunami waveforms for a fault with slip extending up to the trench axis having 66 subfaults (strike wise: 11; dip wise: 6 subfaults). The depths of subfaults are in the range of 9.2–44.1 km. (b and c) Similar to Figure 3a but for 55 subfaults in the depth range of 12.4–44.1 km and 44 subfaults in the depth range of 14.7–44.1 km. Rupture velocity is 3.0 km/s for all three cases. *h* stands for subfault's depth. One week aftershocks ($M > 4$) are from the USGS catalog. The depth values shown in this figure are measured from sea surface.

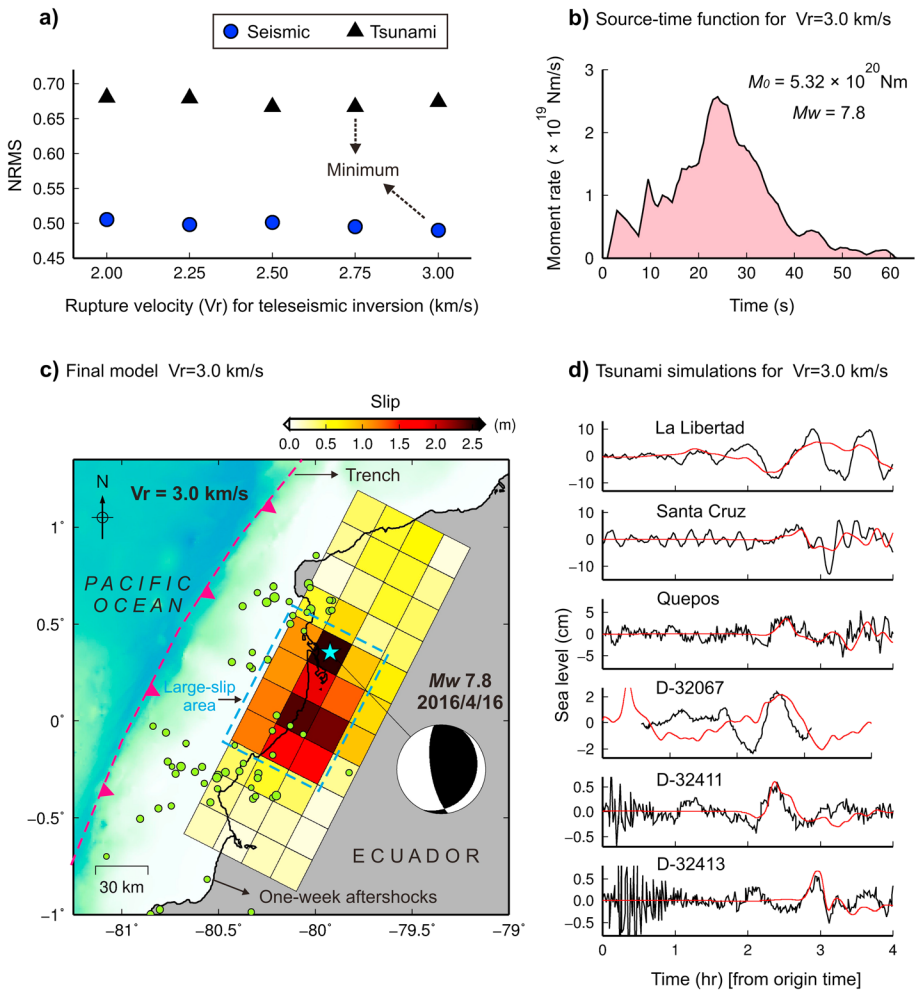

Figure 4. Final source model. (a) NRMS misfits from teleseismic and tsunami simulations. (b) Source-time function for the final model with 44 subfaults whose depths are in the range of 14.7–44.1 km. Rupture velocity is 3.0 km/s. (c) Slip distribution for the final model. The dashed blue rectangle is the large-slip area which stands for subfaults with slip more than 1.5 times of the average slip. The depth range of the large-slip area is 14.7–34.7 km. (d) Comparison of observed and simulated waveforms for the final source model. One week aftershocks ($M > 4$) are from the USGS catalog.

fault at the depth of ~44 km (Figure 4 and Table S1). To study the relationship between maximum rupture front velocity (i.e., assumed velocity) and physical rupture velocity, we plotted snapshots for various V_r (Figure S5) and realized that the assumed velocity (blue curves in Figure S5) and the physical rupture velocity (actual snapshots in Figure S5) are almost identical.

Tsunami simulations revealed that the initial early peak still exists for the 55-subfault model (i.e., 11×5 in Figure 3b), while it disappeared for the 44-subfault model (i.e., 11×4 in Figure 3c). The tsunami NRMS misfits were 0.937 (for 11×6), 0.892 (for 11×5), and 0.674 (for 11×4) indicating that the fit between tsunami observations and simulations was significantly improved for the 44-subfault model. By using the deep fault (i.e., 11×4; Figure 3c), it can be seen that not only the tsunami DART records are reproduced well, but also the simulated waveform at the Santa Cruz tide gauge station was significantly improved (i.e., the first wave was reproduced well; Figure 3c). Therefore, the deep fault with depth range of 14.7–44.1 km is the best fault satisfying both seismic and tsunami observations (Figure 3c). We note that the tsunami waves observed at DARTs 32411 and 32413 (located at ~1400 and ~1800 km from the epicenter) between 2 and 3 h after the origin time are different from that of DART 32067 (located at ~160 km) around the same time interval (Figure 1d). While the former waves are direct tsunami waves, the latter ones are from bathymetric effects; this is possibly the reason that the DART 32067 record is not modeled well between 2 and 3 h. For the

DART 32067, the direct tsunami waves arrived within first 30 min from the origin time because this DART is located very close to the epicenter.

To finalize the slip model, we performed teleseismic inversion using the 44-subfault model by changing V_r from 2.0 to 3.0 km/s at 0.25 km/s intervals. The NRMS misfits for teleseismic or tsunami results revealed that they are close to each other for different V_r (Figure 4a). The minimum NRMS misfit for teleseismic and tsunami results was obtained for models $V_r = 3.0$ km/s and $V_r = 2.75$ km/s, respectively (Figure 4a). Here we report the model $V_r = 3.0$ km/s as the final model because NRMS misfits are smaller for teleseismic than tsunami waveforms.

The final slip model is shown in Figure 4c, and its details including locations of subfaults and slip values are given in Table S1. The western shallowest limit of the slip area is located at the distance of ~60 km from the trench axis. The fault depth is in the range of 14.7–44.1 km. Earthquake rupture lasted for ~60 s, and the maximum moment rate occurred at ~25 s (Figure 4b). Average slip is 0.7 m (average of all nonzero slip subfaults) with a maximum slip of 2.5 m located near the epicenter. The seismic moment is 5.32×10^{20} Nm, corresponding to $M_w = 7.8$. Assuming that large-slip area is defined as subfaults with slip values larger than 1.5 times of the average slip [*Murotani et al*., 2013], the large-slip area is 80 km (along strike) × 60 km (along dip) located to the south of the epicenter (blue dashed rectangle in Figure 4c) at a depth range of 14.7–34.7 km. Average slip on the large-slip area is 1.7 m. The large-slip area together with the aftershock distribution confirms that the rupture propagated southward from the epicenter. Figure 4c shows that the aftershocks are mostly located on the borders of the large-slip area. *Ye et al*. [2016a] noted that aftershocks extended to the trench axis and interpreted that shallower aftershocks were triggered by updip after slip.

The source region of the 2016 earthquake is similar to that of the 1942 earthquake, which also generated moderate tsunami damage. The 1942 event was studied by *Mendoza and Dewey* [1984], *Beck and Ruff* [1984], *Swenson and Beck* [1996], and *Collot et al*. [2004]. The seismic moment of the 1942 event was estimated at $6–8 \times 10^{20}$ Nm (equivalent to M_w 7.8–7.9) with a source-time function showing majority of moment release within the first 24 s [*Swenson and Beck*, 1996]. An average slip of ~1.2 m was reported for the 1942 event by using simple calculations based on the earthquake moment magnitude, whereas it was speculated that the local slip could be much larger [*Swenson and Beck*, 1996]. Three month aftershocks of the 1942 earthquake, from *Mendoza and Dewey* [1984], are shown in Figure S6. All the available information about the 1942 earthquake indicate that it looks similar to the 2016 earthquake in terms of earthquake size (seismic moment), slip amounts, and aftershock locations (Figure S6). The time interval between the 1942 and 2016 earthquakes is 74 years which corresponds to an average slip accumulation of 1.85–3.4 m by assuming a plate convergence rate in the range of 2.5–4.6 cm/yr and given that the plate coupling is high. The accumulated slip in 74 years would be smaller if the plate coupling is low. The average slip calculated for the 2016 event (i.e., 1.7 m) is close to the accumulated slip for low convergence rate (i.e., ~2.5 cm/yr) with high coupling or high convergence rate (i.e., ~4.6 cm/yr) with low coupling, indicating that the 2016 earthquake possibly has released most of the interseismic slip accumulated at this segment of the subduction zone.

In this study, we assumed that initial sea surface heights are equivalent to the coseismic seafloor deformation. Because the slip area and seafloor deformation near trench are narrow (arrow X1 in Figure 2c), it is important to examine whether such narrow coseismic seafloor deformation is equivalent to initial sea surface height or not and what are the effects on tsunami simulations. Figure S7 shows the coseismic seafloor deformation and initial sea surface height (by applying *Kajiura* [1963] filter) for the 66-subfault model ($V_r = 2.0$ km/s). The initial sea surface height is smoother than the coseismic seafloor deformation. Although sharp edges existing in the coseismic seafloor deformation (red arrow in Figure S7) are filtered out in the initial sea surface height, the main features remain the same for both. Especially, the small uplift near trench exists in both. Tsunami simulations revealed that the simulated waveforms are almost the same for both (red and blue waveforms in Figure S7).

4. Conclusions

We studied the source of the 16 April 2016 M_w 7.8 Ecuador earthquake using teleseismic and tsunami observations and applying teleseismic body wave inversion and tsunami modeling. Main findings are as follows:

1. The 2016 Ecuador tsunami registered a maximum zero-to-peak amplitude of ~10 cm on tide gauges and 0.5–2 cm on DART stations.

2. Teleseismic body wave inversions using various subfault numbers, with and without shallow-slip areas (<14.7 km), produced similar synthetic waveforms, while tsunami simulations favored a source model without shallow-slip area.
3. The final slip model lacks the slip in shallow region, with the depth range of 14.7–44.1 km, and the western border of the fault plane is located at the distance of ~60 km from the trench axis. The maximum and average slip values are 2.5 and 0.7 m, respectively. The large-slip area is 80 km (along strike) × 60 km (along dip) located to the south of the epicenter indicating southward propagation of the earthquake rupture. Average slip on the large-slip area, in the depth range of 14.7–34.7 km, is 1.7 m.

Acknowledgments
We downloaded tide gauge data from the Intergovernmental Oceanographic Commission's website (http://www.ioc-sealevelmonitoring.org/). DART data were also downloaded from the website of NOAA on 16 April 2016 (http://nctr.pmel.noaa.gov/Dart/). We downloaded teleseismic records of the earthquakes from Incorporated Research Institutions for Seismology website at http://www.iris.edu/wilber3/find_event. We used the teleseismic body wave inversion program from http://wwweic.eri.u-tokyo.ac.jp/ETAL/KIKUCHI/. Earthquake focal mechanism data of Global Centroid-Moment-Tensor Project (GCMT) were used in this study (http://www.globalcmt.org/). All figures were drafted by using the GMT software [*Wessel and Smith*, 1998]. We are grateful to Andrew Newman (Editor), Thorne Lay (University of California Santa Cruz), and an anonymous reviewer for constructive review comments.

References

Ando, M. (1975), Source mechanism and tectonic significance of historical earthquakes along the Nankai trough, Japan, *Tectonophysics*, *27*, 119–140.

Arreaga-Vargas, P., M. Ortiz, and S. F. Farreras (2005), Mapping the possible tsunami hazard as the first step towards a tsunami resistant community in Esmeraldas, Ecuador, in *Tsunamis*, pp. 203–215, Springer, Netherlands.

Beck, S. L., and L. J. Ruff (1984), The rupture process of the great 1979 Colombia earthquake: Evidence for the asperity model, *J. Geophys. Res.*, *89*, 9281–9291, doi:10.1029/JB089iB11p09281.

Collot, J.-Y., B. Marcaillou, F. Sage, F. Michaud, W. Agudelo, P. Charvis, D. Graindorge, M.- A. Gutscher, and G. Spence (2004), Are rupture zone limits of great subduction earthquakes controlled by upper plate structures? Evidence from multichannel seismic reflection data acquired across the northern Ecuador–southwest Colombia margin, *J. Geophys. Res.*, *109*, B11103, doi:10.1029/2004JB003060.

Fujii, Y., and K. Satake (2008), Tsunami waveform inversion of the 2007 Bengkulu, southern Sumatra, earthquake, *Earth Planets Space*, *60*(9), 993–998.

Geoware (2011), The tsunami travel times (TTT). [Available at http://www.geoware-online.com/tsunami.html.]

Gusman, A. R., S. Murotani, K. Satake, M. Heidarzadeh, E. Gunawan, S. Watada, and B. Schurr (2015), Fault slip distribution of the 2014 Iquique, Chile, earthquake estimated from ocean-wide tsunami waveforms and GPS data, *Geophys. Res. Lett.*, *42*, 1053–1060, doi:10.1002/2014GL062604.

Hayes, G. P., D. J. Wald, and R. L. Johnson (2012), Slab1. 0: A three-dimensional model of global subduction zone geometries, *J. Geophys. Res.*, *117*, B01302, doi:10.1029/2011JB008524.

Heidarzadeh, M., A. R. Gusman, T. Harada, and K. Satake (2015), Tsunamis from the 29 March and 5 May 2015 Papua New Guinea earthquake doublet (M_w 7.5) and tsunamigenic potential of the New Britain trench, *Geophys. Res. Lett.*, *42*, 5958–5965, doi:10.1002/2015GL064770.

Heidarzadeh, M., S. Murotani, K. Satake, T. Ishibe, and A. R. Gusman (2016a), Source model of the 16 September 2015 Illapel, Chile M_w 8.4 earthquake based on teleseismic and tsunami data, *Geophys. Res. Lett.*, *43*, 643–650, doi:10.1002/2015GL067297.

Heidarzadeh, M., T. Harada, K. Satake, T. Ishibe, and A. R. Gusman (2016b), Comparative study of two tsunamigenic earthquakes in the Solomon Islands: 2015 M_w 7.0 normal-fault and 2013 Santa Cruz M_w 8.0 megathrust earthquakes, *Geophys. Res. Lett.*, *43*, 4340–4349, doi:10.1002/2016GL068601.

Inazu, D., and T. Saito (2014), Two subevents across the Japan Trench during the 7 December 2012 off Tohoku earthquake (M_w 7.3) inferred from offshore tsunami records, *J. Geophys. Res. Solid Earth*, *119*, 5800–5813, doi:10.1002/2013JB010892.

Intergovernmental Oceanographic Commission, et al. (2014), *Centenary Edition of the GEBCO Digital Atlas*, published on CD-ROM on behalf of the Intergovernmental Oceanographic Commission and the International Hydrographic Organization as part of the General Bathymetric Chart of the Oceans, British Oceanographic Data Centre, Liverpool, U. K.

Kajiura, K. (1963), The leading wave of a tsunami, *Bull. Earthquake Res. Inst.*, *41*, 535–571.

Kanamori, H., and J. W. Given (1981), Use of long-period surface waves for rapid determination of earthquake-source parameters, *Phys. Earth Planet. Int.*, *27*(1), 8–31.

Kanamori, H., and K. C. McNally (1982), Variable rupture mode of the subduction zone along the Ecuador-Colombia coast, *Bull. Seismol. Soc. Am.*, *72*(4), 1241–1253.

Kennett, B. L. N., E. R. Engdahl, and R. Buland (1995), Constraints on seismic velocities in the Earth from travel times, *Geophys. J. Int.*, *122*, 108–124.

Kikuchi, M., and H. Kanamori (1991), Inversion of complex body waves—III, *Bull. Seismol. Soc. Am.*, *81*(6), 2335–2350.

Kikuchi M., and H. Kanamori (2003), Note on teleseismic body-wave inversion program. [Available at http://www.eri.u-tokyo.ac.jp/ETAL/KIKUCHI/.]

Kreemer, C., G. Blewitt, and F. Maerten (2006), Co-and postseismic deformation of the 28 March 2005 Nias M_w 8.7 earthquake from continuous GPS data, *Geophys. Res. Lett.*, *33*, L07307, doi:10.1029/2005GL025566.

Laske, G., G. Masters, Z. Ma, and M. Pasyanos (2013), Update on CRUST1.0—A 1-degree global model of Earth's crust, Geophys. Res. Abstracts, 15, Abstract EGU2013-2658.

Lay, T., H. Yue, E. E. Brodsky, and C. An (2014), The 1 April 2014 Iquique, Chile, M_w 8.1 earthquake rupture sequence, *Geophys. Res. Lett.*, *41*, 3818–3825, doi:10.1002/2014GL060238.

Li, L., T. Lay, K. F. Cheung, and L. Ye (2016), Joint modeling of teleseismic and tsunami wave observations to constrain the 16 September 2015 Illapel, Chile, M_w 8.3 earthquake rupture process, *Geophys. Res. Lett.*, *43*, 4303–4312, doi:10.1002/2016GL068674.

McCloskey, J., S. S. Nalbant, and S. Steacy (2005), Indonesian earthquake: Earthquake risk from co-seismic stress, *Nature*, *434*(7031), 291–291.

Mendoza, C., and J. W. Dewey (1984), Seismicity associated with the great Colombia-Ecuador earthquakes of 1942, 1958, and 1979: Implications for barrier models of earthquake rupture, *Bull. Seismol. Soc. Am.*, *74*(2), 577–593.

Murotani, S., K. Satake, and Y. Fujii (2013), Scaling relations of seismic moment, rupture area, average slip, and asperity size for $M \sim 9$ subduction-zone earthquakes, *Geophys. Res. Lett.*, *40*, 5070–5074, doi:10.1002/grl.50976.

Okada, Y. (1985), Surface deformation due to shear and tensile faults in a half-space, *Bull. Seismolo. Soc. Am.*, *75*, 1135–1154.

Saito, T., and T. Furumura (2009), Three-dimensional tsunami generation simulation due to sea-bottom deformation and its interpretation based on the linear theory, *Geophys. J. Int.*, *178*, 877–888.

Satake, K. (1987), Inversion of tsunami waveforms for the estimation of a fault heterogeneity: Method and numerical experiments, *J. Phys. Earth*, *35*(3), 241–254.

Satake, K. (1995), Linear and nonlinear computations of the 1992 Nicaragua earthquake tsunami, *Pure Appl. Geophys.*, *144*, 455–470.
Satake, K., and B. Atwater (2007), Long-term perspectives on giant earthquakes and tsunamis at subduction zones, *Annu. Rev. Earth Planet. Sci.*, *35*, 349–374.
Soloviev, L., and N. Go (1975), *A Catalogue of Tsunamis on the Eastern Shore of the Pacific Ocean (1513–1968)*, 204 pp., Nauka House, Moscow, USSR.
Stein, S., and E. A. Okal (2007), Ultra-long period seismic study of the December 2004 Indian Ocean earthquake and implications for regional tectonics and the subduction process, *Bull. Seismol. Soc. Am.*, *97*, S279–S295.
Swenson, J. L., and S. L. Beck (1996), Historical 1942 Ecuador and 1942 Peru subduction earthquakes and earthquake cycles along Colombia-Ecuador and Peru subduction segments, *Pure Appl. Geophys.*, *146*(1), 67–101.
Synolakis, C. E. (2003), Tsunami and seiche, in *Earthquake Engineering Handbook*, chap. 9, edited by W. F. Chen and C. Scawthorn, pp. 1–90, CRC Press, Boca Raton, Fla.
Trenkamp, R., J. N. Kellogg, J. T. Freymueller, and H. P. Mora (2002), Wide plate margin deformation, southern Central America and northwestern South America, CASA GPS observations, *J. South Am. Earth Sci.*, *15*(2), 157–171.
Weatherall, P., K. M. Marks, M. Jakobsson, T. Schmitt, S. Tani, J. E. Arndt, M. Rovere, D. Chayes, V. Ferrini, and R. Wigley (2015), A new digital bathymetric model of the world's oceans, *Earth Space Sci.*, *2*, 331–345, doi:10.1002/2015EA000107.
Wessel, P., and W. H. F. Smith (1998), New, improved version of Generic Mapping Tools released, *Eos Trans. AGU*, *79*(47), 579, doi:10.1029/98EO00426.
Yamazaki, Y., T. Lay, K. F. Cheung, H. Yue, and H. Kanamori (2011), Modeling near-field tsunami observations to improve finite-fault slip models for the 11 March 2011 Tohoku earthquake, *Geophys. Res. Lett.*, *38*, L00G15, doi:10.1029/2011GL049130.
Ye, L., H. Kanamori, J. P. Avouac, L. Li, K. F. Cheung, and T. Lay (2016a), The 16 April 2016, M_w 7.8 (M_s 7.5) Ecuador earthquake: A quasi-repeat of the 1942 M_s 7.5 earthquake and partial re-rupture of the 1906 M_s 8.6 Colombia–Ecuador earthquake, *Earth Planet. Sci. Lett.*, *454*, 248–258.
Ye, L., H. Kanamori, J. P. Avouac, L. Li, K. F. Cheung, and T. Lay (2016b), Corrigendum to "The 16 April 2016, M_w 7.8 (M_s 7.5) Ecuador earthquake: A quasi-repeat of the 1942 M_s 7.5 earthquake and partial re-rupture of the 1906 M_s 8.6 Colombia–Ecuador earthquake", *Earth Planet. Sci. Lett.*, *454*, 248–258.